GPS measurements of crustal uplift near Jakobshavn Isbræ due to glacial ice mass loss

Shfaqat Abbas Khan,[1] Lin Liu,[2] John Wahr,[2] Ian Howat,[3] Ian Joughin,[4] Tonie van Dam,[5] and Kevin Fleming[6]

Received 19 February 2010; revised 30 April 2010; accepted 11 May 2010; published 16 September 2010.

[1] We analyze 2006–2009 data from four continuous Global Positioning System (GPS) receivers located between 5 and 150 km from the glacier Jakobshavn Isbræ, West Greenland. The GPS stations were established on bedrock to determine the vertical crustal motion due to the unloading of ice from Jakobshavn Isbræ. All stations experienced uplift, but the uplift rate at Kangia North, only 5 km from the glacier front, was about 10 mm yr^{-1} larger than the rate at Ilulissat, located only ~45 km further away. This suggests that most of the uplift is due to the unloading of the Earth's surface as Jakobshavn thins and loses mass. Our estimate of Jakobshavn's contribution to uplift rates at Kangia North and Ilulissat are 14.6 ± 1.7 mm yr^{-1} and 4.9 ± 1.1 mm yr^{-1}, respectively. The observed rates are consistent with a glacier thinning model based on repeat altimeter surveys from NASA's Airborne Topographic Mapper (ATM), which shows that Jakobshavn lost mass at an average rate of 22 ± 2 km^3 yr^{-1} between 2006 and 2009. At Kangia North and Ilulissat, the predicted uplift rates computed using thinning estimates from the ATM laser altimetry are 12.1 ± 0.9 mm yr^{-1} and 3.2 ± 0.3 mm yr^{-1}, respectively. The observed rates are slightly larger than the predicted rates. The fact that the GPS uplift rates are much larger closer to Jakobshavn than further away, and are consistent with rates inferred using the ATM-based glacier thinning model, shows that GPS measurements of crustal motion are a potentially useful method for assessing ice-mass change models.

Citation: Khan, S. A., L. Liu, J. Wahr, I. Howat, I. Joughin, T. van Dam, and K. Fleming (2010), GPS measurements of crustal uplift near Jakobshavn Isbræ due to glacial ice mass loss, *J. Geophys. Res.*, *115*, B09405, doi:10.1029/2010JB007490.

1. Introduction

[2] Greenland's main outlet glaciers have more than doubled their contribution to global sea-level rise over the past decade [*Rignot and Kanagaratnam*, 2006; *Rignot et al.*, 2008]. Jakobshavn Isbræ in West Greenland is Greenland's largest outlet glacier in terms of drainage area, draining ~6.5% of the ice sheet [*Krabill et al.*, 2000]. Using synthetic aperture radar data, *Joughin et al.* [2004] found that the velocity of Jakobshavn Isbræ doubled between 1992 and 2003. More recent measurements have shown that there has been a steady increase in the flow rate over the glacier's faster-moving region of ~5% yr^{-1} [*Joughin et al.*, 2008a, 2008b]. Airborne laser altimeter surveys of Jakobshavn Isbræ have revealed dynamic thinning of up to 10 m yr^{-1} between 1997 and 2003 [*Krabill et al.*, 2004], while repeat surveys between 2002 and 2006 have found that thinning rates have increased, with the thinning zone migrating inland [*Joughin et al.*, 2008b].

[3] Jakobshavn Isbræ's acceleration has been attributed to the collapse of much of its floating tongue [*Joughin et al.*, 2004; *Thomas*, 2004; *Dietrich et al.*, 2007; *Joughin et al.*, 2008a; *Thomas et al.*, 2009]. This collapse might have been due to enhanced sub-ice shelf melting driven by an influx of warm water [*Holland et al.*, 2008], and to increased calving caused by sea ice reduction in the fjord [*Joughin et al.*, 2008b; *Amundson et al.*, 2010]. The current episode of accelerated flow and thinning might now be self-sustaining due to a landward-deepening bed slope [*Clarke and Echelmeyer*, 1996], and could continue for centuries to come [*Joughin et al.*, 2008b].

[4] Glacial thinning reduces the load on the Earth's surface and thus causes crustal uplift. Earlier studies, e.g., *Larsen et al.* [2004, 2005], measured rapid crustal uplift in southeast

[1]DTU Space-National Space Institute, Department of Geodesy, Copenhagen, Denmark.
[2]Department of Physics and Cooperative Institute for Research in Environmental Sciences, University of Colorado at Boulder, Boulder, Colorado, USA.
[3]School of Earth Sciences and Byrd Polar Research Center, Ohio State University, Columbus, Ohio, USA.
[4]Applied Physics Lab, University of Washington, Seattle, Washington, USA.
[5]Department of Physics and Material Sciences, University of Luxembourg, Luxembourg, Luxembourg.
[6]Department of Spatial Sciences, Curtin University of Technology, Perth, Western Australia, Australia.

0148-0227/10/2010JB007490

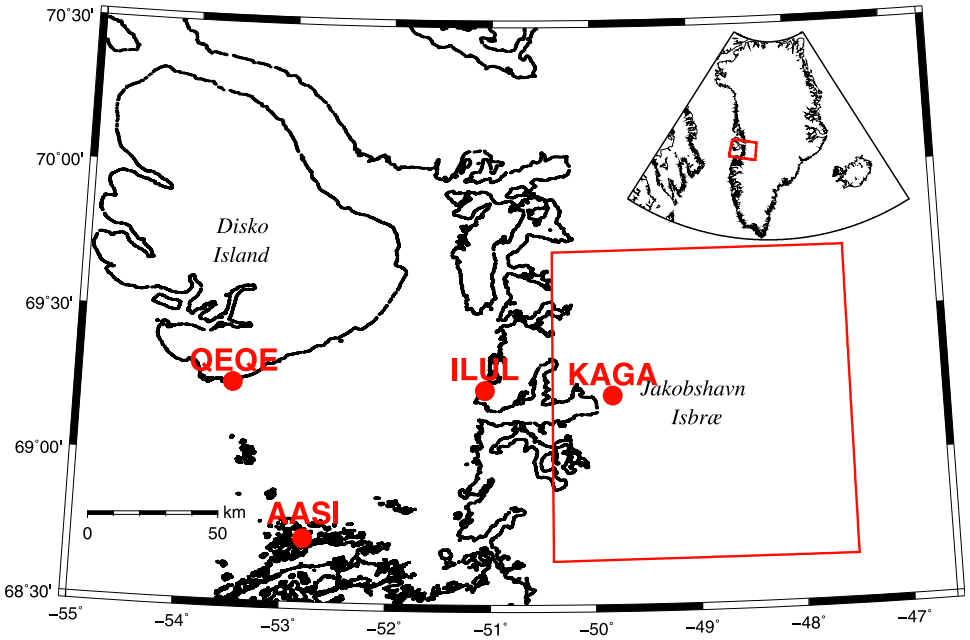

Figure 1. West-central Greenland (outlined by the red box in the inset map) and the GPS locations (red dots, with coordinates listed in Table 1). The large red box marks the area shown in Figure 5a. The coastline data are obtained from the NOAA National Geophysical Data Center, based on World Vector Shoreline database [*Soluri and Woodson*, 1990].

Alaska using continuous Global Positioning System (GPS) measurements. They observed present-day uplift rates up of to 32 mm/yr caused by post-Little Ice Age glacial retreat and present-day ongoing ice mass loss. Other studies have used GPS measurements of crustal uplift to place constraints on the present-day ice mass loss of glaciers in coastal Alaska [*Sauber and Molnia*, 2004], Svalbard [*Sato et al.*, 2006], southeast Greenland [*Khan et al.*, 2007], and Patagonia [*Dietrich et al.*, 2010]. The amplitude of the uplift depends on the amount of mass lost from the glacier in question, and on the distance between the load and the observation point.

[5] Here, we use GPS measurements from 2006–2009 to study vertical crustal motion near Jakobshavn Isbræ. We use data from four continuously operating GPS receivers located on bedrock between 5 and 150 km of Jakobshavn Isbræ to assess a glacial surface elevation change map constructed using repeat laser altimetry surveys from NASA's Airborne Topographic Mapper (ATM) [*Krabill et al.*, 2004]. The goal of our GPS analysis is to isolate the part of the loading signal caused by mass changes of Jakobshavn Isbræ and its catchment. We also use glacial-loading models, including the ICE-5G/VM2 postglacial rebound model from *Peltier* [2004] and a Greenland ice mass loss model from *Velicogna* [2009], to assess and minimize the contamination of our GPS signal from other geophysical processes and areas of mass change. Note that because we have only a few years of GPS data, and because mass loss rates and the associated crustal response are likely to be evolving with time, our results should not be interpreted as long-term trends.

[6] Here, we do not study horizontal motion due to the difficulty of quantitatively and unambiguously assessing uncertainties in horizontal motions caused by possible errors in ATM and postglacial rebound model.

2. GPS Network

[7] In December 2005, the Danish Technical University (DTU Space) established the GPS station QEQE at Qeqertarsuaq (Figure 1), ~150 km from Jakobshavn Isbræ's 2007 summer calving front. Two additional stations, AASI (Aasiaat) and ILUL (Ilulissat) were established in September 2005 by DTU Space and the University of Luxembourg, ~130 km (AASI) and ~45 km (ILUL) from the calving front. In May 2006, the University of New Hampshire, the University of Alaska Fairbanks, and UNAVCO (University NAVSTAR Consortium) established a station, KAGA (Kangia North), on the north side of Jakobshavn Isbræ, ~5 km upstream from the 2007 summer calving front. All stations are set on bedrock and operate continuously, with data downloaded daily via telemetry. ILUL and AASI consist of an LEIAT504 antenna with radome, while QEQE consists of an ASH701945E_M antenna with radome. The original antenna at KAGA, a TRM41249.00, was replaced on August 2, 2007, by a TRM29659.00 antenna with radome. No antenna replacements were carried out at the other three sites. We use all data spanning the time when each station was established through September 2009.

3. GPS Data Analysis and Results

[8] To estimate site coordinates, we use the GIPSY OASIS 5.0 software package [*Zumberge et al.*, 1997] developed at the Jet Propulsion Laboratory (JPL). The orbit products we

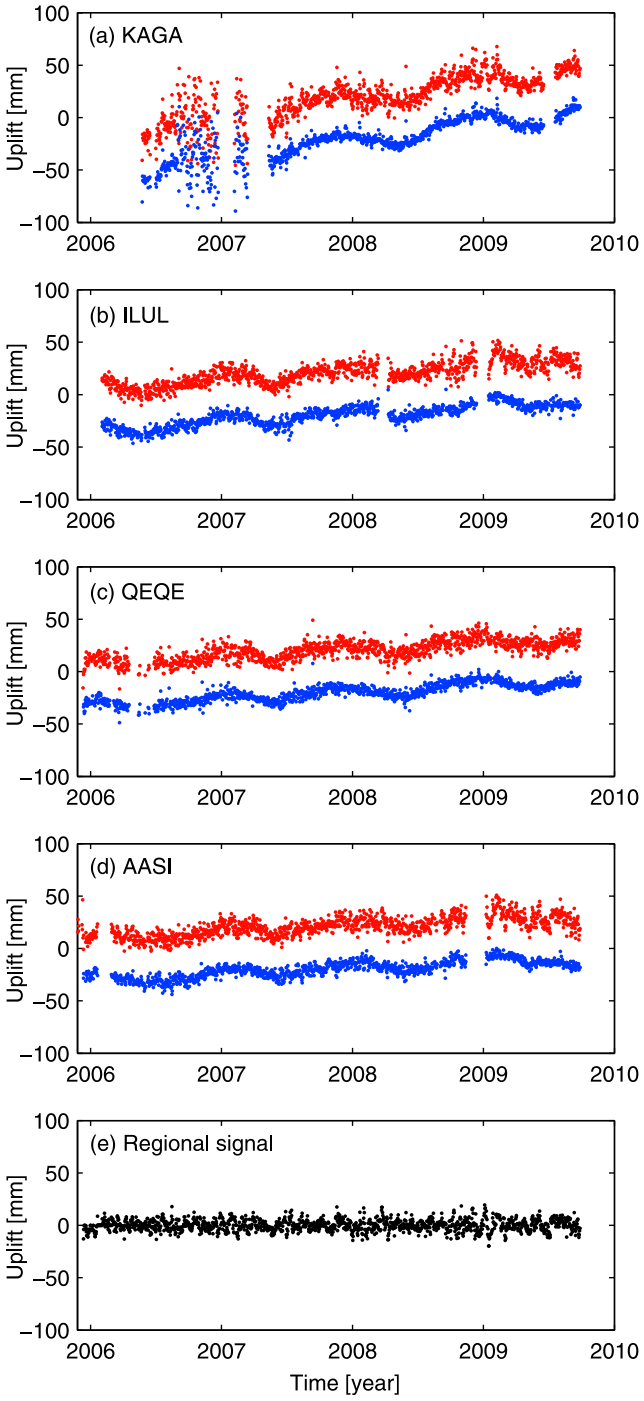

Figure 2. (a–d) Daily values of vertical positions at the four stations before (red dots) and after (blue dots) regional filtering. The time series of daily vertical positions before and after filtering are shifted by an offset, for clarity. (e) Daily values of the regional signal (see section 3.1).

use were released in 2009 by JPL and include satellite orbits, satellite clock parameters, and earth orientation parameters. The new orbit products take the satellite antenna phase center offsets into account. We correct for the antenna phase center offsets of the transmitters (satellites) and receivers (ground stations) using the absolute International GNSS Service (IGS) antenna correction file (the igs051525.atx Antex file). Receiver clock parameters are modeled, and the atmospheric delay parameters are modeled using the Global Mapping Function (GMF) [*Boehm et al.*, 2006a], with an elevation cut-off angle of 5°. The impact of the minimum elevation angle and the type of mapping function on the inferred uplift rates is described in section 3.2. Corrections are applied to remove the solid earth tide and ocean tidal loading. The amplitudes and phases of the main ocean tidal loading terms are calculated using the online program provided by H.-G. Scherneck and M. S. Bos (available at http://www.oso.chalmers.se/~loading) applied to the GOT00.2 [*Ray*, 1999] ocean tide model. Site coordinates for each day are obtained using the GIPSY OASIS 5.0 Precise Point Positioning (PPP) strategy. The site coordinates are computed in the non-fiducial frame and transformed to the IGS2005 frame [*Altamimi et al.*, 2007]. The transformation parameters (x-files) from the free-network estimates to the IGS2005 reference frame for a particular day are provided by JPL (ftp://sideshow.jpl.nasa.gov/pub/JPL_GPS_Products/Final/).

3.1. Regional Filtering of the GPS Data

[9] Several methods have been designed to reduce spatially-correlated noise in GPS data. Earlier studies such as *Wdowinski et al.* [1997] used a stacking method based on computing a daily common mode to improve the signal-to-noise ratio. *Johansson et al.* [2002] investigated the use of Empirical Orthogonal Function (EOF) analysis for the same purpose. In analyzing the time series of the horizontal position estimates, *Davis et al.* [2006] used a statistical approach that allowed for the estimation of nuisance parameters (mainly seasonal variations) when changes in velocity occur over the length of the time series. Here, we apply a 'regional filter' [*Khan et al.*, 2008] to the GPS data to reduce spatially correlated errors (or regional common modes) due to e.g., tropospheric modeling errors and satellite orbit errors.

[10] We apply this regional filter only to remove common modes at periods shorter than 90 days. Spatially correlated annual and inter-annual variations are thus not removed. We smooth the GPS time series using a moving average (averaging over 90 days), and we subtract these smoothed results from the original data to obtain a high-frequency time series. We then fit a temporal model consisting of an offset (only for KAGA, to correct for the August, 2007 antenna change), linear, and annually varying terms and remove the modeled values from each high-frequency time series to obtain residual time series. The residual time series at the four GPS stations are then averaged together to obtain a regional-averaged high-frequency time series, which is removed from the original set of daily values at each station.

[11] The effects of regional filtering are illustrated in Figure 2, which shows the daily values of vertical position at each of the GPS stations before and after the regional filtering is applied (Figures 2a–2d), denoted by the red and blue dots, respectively. The time series are separated by an offset simply for clarity. Figure 2e shows the regional signal. There is a clear reduction in the scatter after applying the regional filter, while the secular, annual, and inter-annual signals are unchanged.

[12] In addition to spatially-correlated errors, GPS time series have error sources that produce temporal correlations in the data. Various methods have been employed to take

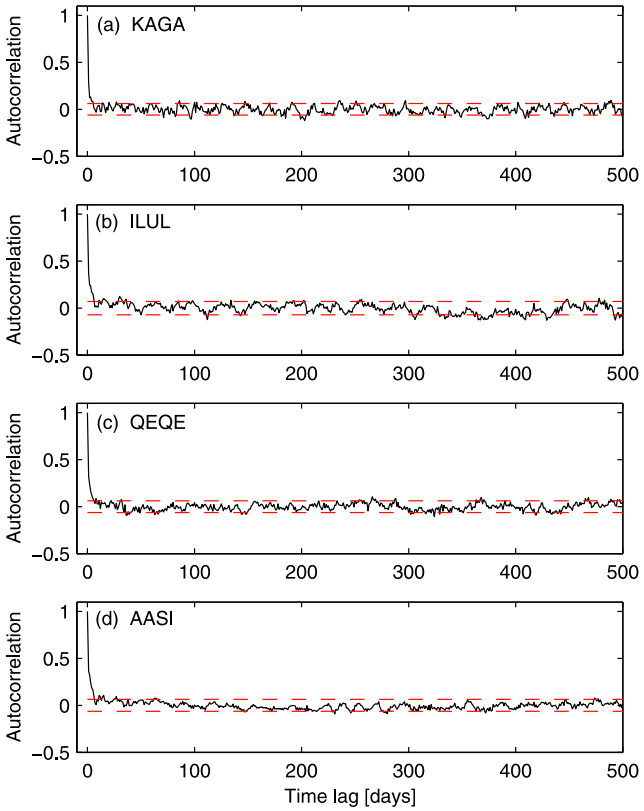

Figure 3. Autocorrelation functions of residuals (the residuals are obtained by removing an offset (only at KAGA), annual, and linear terms from the regionally filtered daily solutions) at (a) KAGA, (b) ILUL, (c) QEQE, and (d) AASI. The time lag is given in days and the autocorrelation is normalized to 1 at time lag = 0. The dashed horizontal lines denote the 95% confidence band centered at zero.

temporally correlated (non-Gaussian) noise into account when analyzing GPS data. *Williams et al.* [2004], for example, analyzed GPS data for noise content using Maximum Likelihood Estimation (discussed further in section 4). Here, we use a method of determining linear rates in GPS time series in the presence of correlated noise described by *Khan et al.* [2008]. By computing autocorrelations of the residual GPS vertical solutions after regional filtering, we find an error de-correlation time for each station. Figure 3 shows the autocorrelation functions for each site using the regionally-filtered daily residuals. The residuals in this case are obtained by removing an offset (only at KAGA), annual, and linear terms from the regionally filtered vertical solutions.

[13] The time lag, τ, is given in days, and the autocorrelation is normalized to 1 at $\tau = 0$ [*Wahr et al.*, 2001]. The two horizontal lines (dashed lines) denote the 95% confidence band centered at zero; i.e., if the residuals are randomly distributed, all the autocorrelations fall within the 95% confidence limits. Thus, the 95% confidence band can be used to test for randomness and to find the de-correlation time. Figure 3 shows that the autocorrelation functions reach the 95% confidence band when the time lag reaches about 30 days. However, the autocorrelation functions do show peaks slightly beyond the 95% confidence band e.g., between time lags of 300–400 days for ILUL (Figure 3b). This is most likely due to inter-annual variations in the annual term, which for this work we assume to be constant.

[14] We construct 30-day averages of the daily vertical solutions shown in Figure 2 to take the temporally correlated (non-Gaussian) noise into account. We use the root mean square (rms) of those averages to represent their uncertainties. The rms values are typically about 3 mm. However, for data between August 30, 2006 and March 14, 2007, we obtain rms values of 15–30 mm at KAGA (mainly because the GPS receiver collected data for only 1 hour instead of 24 hours each day during this period). Using the 30-day averages and their assigned uncertainties, we simultaneously fit an offset (for KAGA), and annual and linear terms to all time series. Our best-fitting uplift rates when taking the temporally correlated (non-Gaussian) noise into account are 17.1 ± 1.4 mm yr^{-1} (KAGA), 8.5 ± 0.6 mm yr^{-1} (ILUL), 6.6 ± 0.5 mm yr^{-1} (QEQE), and 5.8 ± 0.5 mm yr^{-1} (AASI). The relatively large uncertainty at KAGA is caused by the 2007 antenna replacement (which causes an offset of 1.2 ± 2.3 mm) and by data gaps and noisy data between August 2006 and May 2007, as mentioned above. The fitted uplift rates, annual amplitude and phase values are listed in Table 1.

[15] Figures 4a–4d show the 30-day averages of the GPS vertical solutions and their rms errors. The solid lines show our best-fitting trends, corresponding to the values given in Table 1. Figures 4e–4h show convergence plots for the GPS uplift rates. In these examples, each estimate of the uplift rate is obtained by fitting the same terms discussed previously to the first 300 days of data, then adding the next 30 days and repeating the fit and so forth. Each estimate of the linear term is plotted as a dot and the vertical lines describe the estimated uncertainties of the uplift, with the horizontal dashed lines marking the uplift rates listed in Table 1. None of the convergence plots display annual variations and each station's uplift rate has converged to within the errors bars well before the end of the data span. We conclude that the annual and linear terms are well separated using the existing length of the time series, and that the fitted trends are insensitive to inter-annual, seasonal and other short-term variations, such as those related to snow accumulation and melting.

[16] These uplift rates could include contributions from changes in loading outside of the Jakobshavn Isbræ drainage basin (discussed in section 6), and from unmodeled errors in the orbit, the reference frame, and tropospheric delay estimates. Additionally, long-period orbit and reference frame errors are possible, and would not be entirely removed by the regional filter. This is discussed further in section 6.

Table 1. Observed Uplift Rates and Annual Amplitude and Phase Values (Phase Defined Relative to Jan 1) for the 4 GPS Sites, When Using a 5° Cut-Off Angle and the GMF Mapping Function and 30-Day Averages of the Vertical Solutions

	Rate (mm yr^{-1})	Amplitude (mm)	Phase (deg)
KAGA	17.1 ± 1.4	8.3 ± 1.4	50 ± 12
ILUL	8.5 ± 0.6	5.2 ± 0.8	31 ± 4
QEQE	6.6 ± 0.5	4.3 ± 0.7	19 ± 5
AASI	5.8 ± 0.5	4.8 ± 0.7	20 ± 6

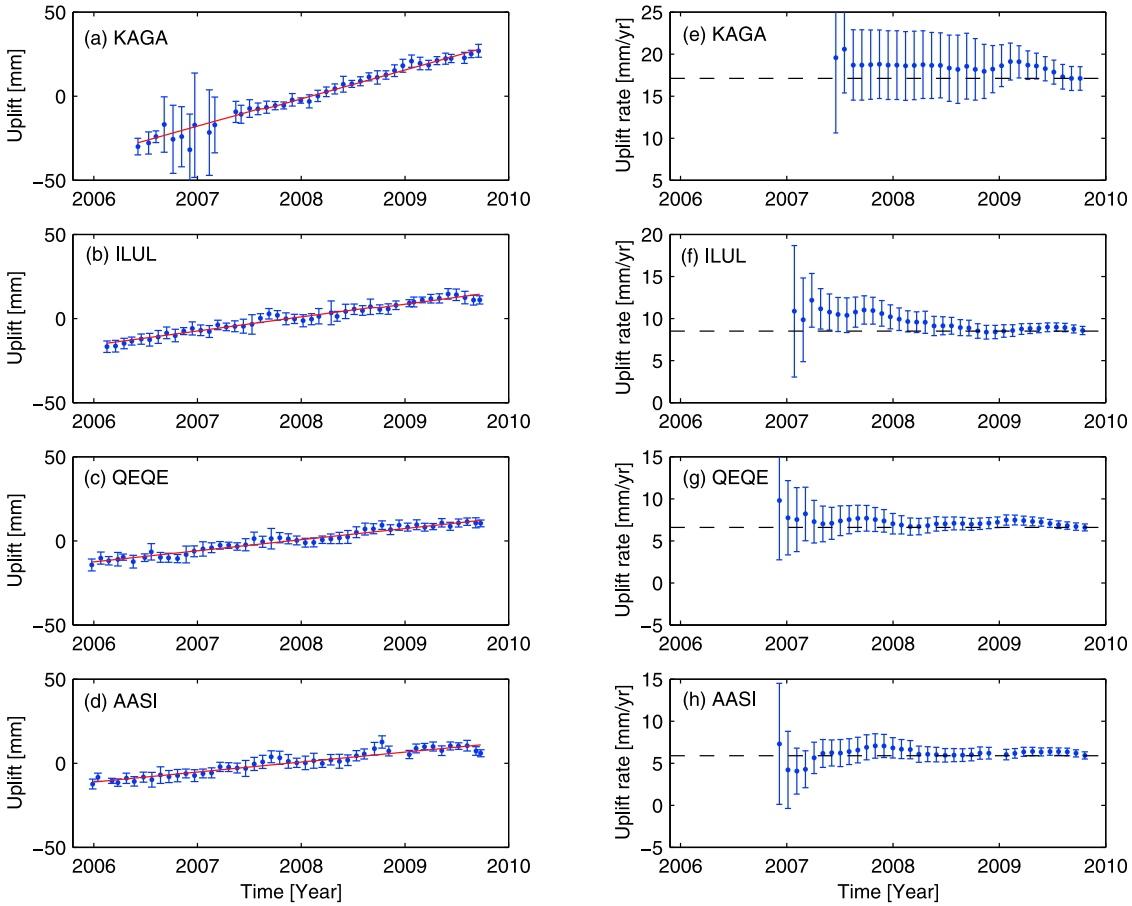

Figure 4. (a–d) The 30-day averages (blue dots) and the linear fit at each station. The vertical bars show the uncertainties in the 30-day values. (e–h) Convergence plots of uplift rates at KAGA, ILUL, QEQE, and AASI. Obtained by fitting an offset (only at KAGA), annual, and linear terms to the first 300 days of data; adding the next 30 days and repeating the fit; etc. Each solution for the linear term is plotted as a dot and the vertical lines describe the estimated uncertainties of the secular uplift. The horizontal dashed lines display the uplift rates listed in Table 1.

3.2. Influence of the Elevation Cut-Off Angle and Mapping Function on the Uplift Rates

[17] The GPS time series used in section 3.1 were obtained using the Global Mapping Function (GMF) [*Boehm et al.*, 2006a] to represent the elevation-dependence of the tropospheric delay, and an elevation cut-off angle of 5°. However, *a priori* zenith hydrostatic delay errors project into GPS height estimates. These errors depend on the elevation cut-off angle and on the elevation angle-dependent data weighting. The associated errors in the estimated station heights are hence latitude dependent because sites at higher latitudes have a greater proportion of low-elevation observations [*Boehm et al.*, 2006b; *Tregoning and Herring*, 2006; *Vey et al.*, 2006].

[18] To study the influence of the choice of mapping function and elevation cut-off angle on the uplift rates, we construct four time series for each station, using combinations of a 5° or 15° cut-off angle, and the GMF mapping function or the Niell Mapping Function (NMF) [*Niell*, 1996], which was used by *Khan et al.* [2008]. All other analysis models and numerical parameters used in the GPS processing are unchanged. Following the same procedure outlined in section 3.1, our best-fitting uplift rates are listed in Table 2. The difference between the highest and lowest uplift

Table 2. Observed Uplift Rates When Using Combinations of Elevation Cut-Off Angles (5° and 15°) and Different Mapping Functions (NMF and GMF)[a]

	5° Cut-Off and Niell	5° Cut-Off and GMF	15° Cut-Off and Niell	15° Cut-Off and GMF
KAGA	17.3 ± 1.4	17.1 ± 1.4	16.5 ± 1.5	16.9 ± 1.4
ILUL	8.6 ± 0.6	8.5 ± 0.6	8.4 ± 0.6	8.3 ± 0.6
QEQE	6.6 ± 0.5	6.6 ± 0.5	6.3 ± 0.5	6.5 ± 0.5
AASI	5.3 ± 0.5	5.8 ± 0.5	4.8 ± 0.5	5.5 ± 0.5

[a]The values in the third column are the same as those in the second column of Table 1 and are listed here for better comparison. Uplift rates are in mm yr^{-1}.

Table 3. Difference in Uplift Rates Between Using 5° and 15° as the Elevation Cut-Off Angle, With the GMF Mapping Function; Using 5° and 15° as the Elevation Cut-Off Angle, With the NMF Mapping Function; Using NMF and GMF as the Mapping Function, With an Elevation Cut-Off Angle of 5°; and Using NMF and GMF as the Mapping Function, With an Elevation Cut-Off Angle of 15°[a]

	GMF Diff (5°–15°)	Niell Diff (5°–15°)	5° Cut-Off Diff (GMF - Niell)	15° Cut-Off Diff (GMF - Niell)
KAGA	0.2	0.8	0.2	0.4
ILUL	0.2	0.2	0.1	0.1
QEQE	0.1	0.3	0.0	0.2
AASI	0.3	0.5	0.5	0.7
Mean	0.2	0.5	0.2	0.4

[a]The uncertainty of the differences is 0.1 mm yr^{-1}. Uplift rates are in mm yr^{-1}.

rates at KAGA, ILUL, QEQE, and AASI are 0.8 mm yr^{-1}, 0.3 mm yr^{-1}, 0.3 mm yr^{-1}, and 1.0 mm yr^{-1}, respectively.

[19] We obtain the highest uplift rates (except for AASI) using the NMF mapping function and an elevation cut-off angle of 5°, and the lowest uplift rates using the NMF mapping function and an elevation cut-off angle of 15°. To determine which combination of elevation cut-off angle and mapping function gives the most consistent results, we calculate and compare differences among the four sets of uplift rates. The second column in Table 3 presents the differences in uplift rates calculated using elevation cut-off angles of 5° and 15° and the GMF mapping function, resulting in a mean difference of 0.2 mm yr^{-1}. The third column in Table 3 shows the differences in uplift rates calculated using the two elevation cut-off angles, but with the NMF mapping function. Here, we obtain a mean difference of 0.5 mm yr^{-1}. It is clear that the GMF mapping function gives more consistent results than the NMF mapping function for different elevation cut-off angles. Similarly, the fourth column in Table 3 shows differences in uplift rates between using NMF and GMF as mapping functions with an elevation cut-off angle of 5°, resulting in a mean difference of 0.2 mm yr^{-1}. Finally, the fifth column in Table 3 shows the differences in uplift rates between using NMF and GMF as mapping function, but for an elevation cut-off angle of 15°. The mean difference for this case is 0.4 mm yr^{-1}, suggesting that the elevation cut-off angle of 5° gives slightly more consistent results than using an elevation cut-off angle of 15°. Thus, uplift rates obtained using an elevation cut-off angle of 5° and the GMF mapping function are used in the rest of this work.

3.3. Long-Period GPS Errors

[20] We note that long-period GPS errors, i.e., unmodeled orbit errors and reference frame errors, would tend to be correlated over long distances, and so would have essentially the same effect at each GPS station. To consider possible orbit errors that might contaminate the estimated vertical displacements, we process the GPS data using orbits, earth orientation parameters, and clock products provided by the Massachusetts Institute of Technology (MIT), and compare the GPS solutions calculated with those using the JPL orbit products as described in section 3. MIT and JPL estimate their products independently from one another and use different approaches. Table 4 (sixth column) presents the uplift rates obtained with MIT products, using an elevation cut-off angle of 5° with the GMF mapping function. The MIT uplift rates are all 0.8 mm yr^{-1} smaller than the JPL rates (Table 4, fifth column) [see also *Khan et al.*, 2010], suggesting that orbit errors have the same effect at each GPS station. That is certainly also true of reference frame errors.

4. Estimating GPS Uplift Rates and Uncertainties Using the MLE Technique

[21] In this section, we use an independent method to estimate uplift rates from the GPS data and their corresponding uncertainties. As discussed in section 3.1, errors in GPS positions are non-Gaussian distributed and are statistically correlated with one another. GPS time series have error sources that introduce temporal correlations into the data. To take the temporally correlated, non-Gaussian noise into account, we analyze the GPS data for white noise plus flicker noise using Maximum Likelihood Estimation (MLE) [*Williams et al.*, 2004]. GPS time series can be described as a power law process [*Mandelbrot*, 1983; *Agnew*, 1992], or one with a time-domain behavior that has a power spectrum of the form (adopted from *Williams et al.* [2004])

$$P_x(f) = P_0\left(\frac{f}{f_0}\right)^{\kappa} \tag{1}$$

where P_x is the power density of the uplift time series, f is the temporal frequency, P_0 and f_0 are normalizing constants, and κ is the spectral index [*Mandelbrot and van Ness*, 1968; *Williams et al.*, 2004]. Classical white noise is obtained for $\kappa = 0$, while $\kappa \neq 0$ refers to colored noise. The special case of $\kappa = -1$ is called 'flicker' noise. Stationary processes with $-1 < \kappa < 1$ are called 'fractional Gaussian' processes. *Williams et al.* [2004] found that the noise in GPS solutions

Table 4. Uplift Rates and Their Related Uncertainties Calculated Assuming Various Stochastic Models When Using a Cut-Off Angle of 5° and the GMF Mapping Function and JPL Orbits and Clock Products[a]

	White Noise Only ($\kappa = 0$)	Flicker Noise ($\kappa = -1$)	Fractional Gaussian ($\kappa = -0.65$)	Fit to Means	MIT
KAGA*	17.3 ± 0.2	18.4 ± 1.6	17.5 ± 0.8	17.2 ± 0.9	16.4 ± 0.9
KAGA	17.4 ± 0.3	18.6 ± 2.2	17.7 ± 1.0	17.1 ± 1.4	16.3 ± 1.5
ILUL	8.7 ± 0.2	8.4 ± 1.5	8.5 ± 0.6	8.5 ± 0.6	7.7 ± 0.6
QEQE	6.4 ± 0.1	6.4 ± 1.1	6.4 ± 0.5	6.6 ± 0.5	5.8 ± 0.6
AASI	5.7 ± 0.1	5.1 ± 1.3	5.4 ± 0.5	5.8 ± 0.5	5.0 ± 0.5

[a]The sixth column shows uplift rates obtained using MIT orbits and clock products. We simultaneously fit an offset (for KAGA), and annual and linear terms to all time series. Asterisk indicates that data between August 30, 2006 and March 14, 2007 are removed.

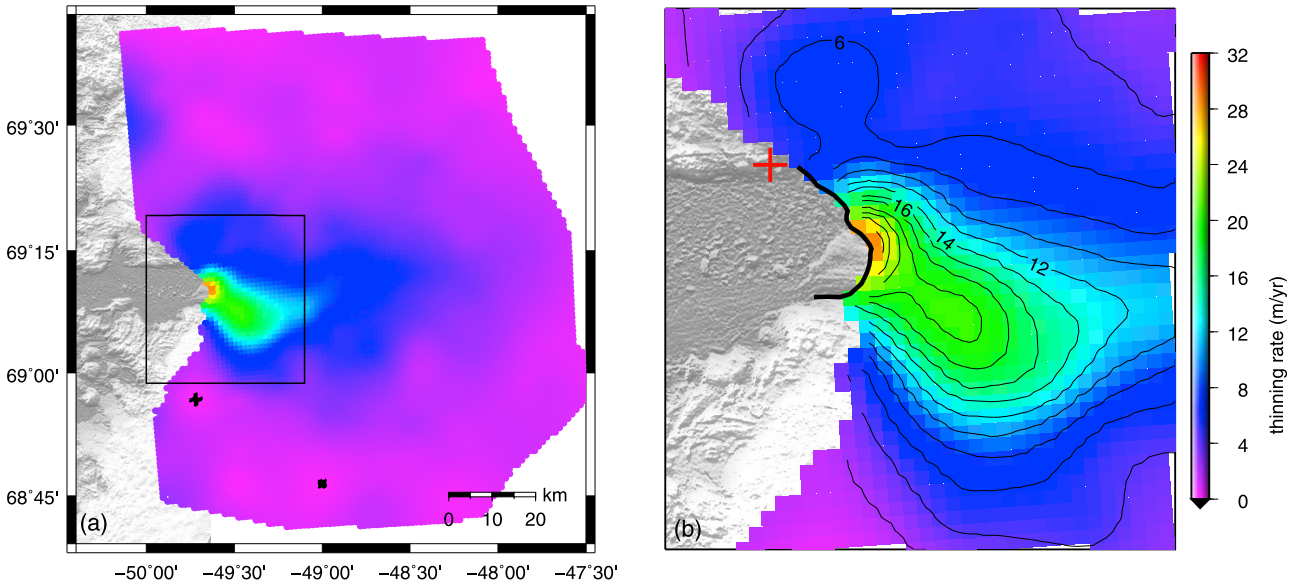

Figure 5. (a) Gridded Jakobshavn Isbræ thinning elevation rates between 2006 and 2009 interpolated from ATM measurements. (b) Close-up of the thinning rates, with contours over the area near the glacier trunk, outlined by the black box in Figure 5a. The thick black line is the grounding line determined from a post-2003 summer Radarsat image. The red cross shows the KAGA GPS site. Background images are shaded topography.

can best be described as a combination of white noise and flicker noise. However, in regional solutions, where a spatially correlated signal has been removed, they obtained a slightly lower mean spectral index. Other studies, e.g., *Teferle et al.* [2008], concluded that the noise in GPS height time series was best described as a combination of white noise and fractional noise. For a network of European Sea Level Service (ESEAS) CGPS network sites, *Teferle et al.* [2008] found that the noise was characterized by a fractal noise process with a spectral index of about −0.7.

[22] Table 4 (second through fifth columns) lists the uplift rates and their uncertainties for the KAGA, ILUL, QEQE, and AASI time series calculated assuming various stochastic models. The results denoted by KAGA were found using all available data, while those denoted as KAGA* using a time series where values from the noisy period of August 30, 2006 to March 14, 2007 have been removed. The fifth column of Table 4 shows uplift rates and their uncertainties estimated as described in section 3 and listed in Tables 2 and 3. For simplicity we denote this method as fitting to means (FTM). Using MLE, and taking into account different spectral indexes, we calculate the uplift rates and uncertainties using the filtered time series shown in Figure 2. We note that the uplift rates are more or less the same when using various stochastic models. However, the related uncertainties are different. For example, if a white noise process is assumed ($\kappa = 0$), the uncertainties are 0.1 mm yr^{-1} for QEQE and AASI, and 0.2 mm yr^{-1} for ILUL. For KAGA, we obtain an uncertainty of 0.3 mm yr^{-1} when using all data and 0.2 mm yr^{-1} when excluding the noisy data (KAGA*). These uncertainties are 5–6 times smaller than the uncertainties obtained using the FTM method. If a flicker noise process is assumed ($\kappa = -1$), the uncertainties become much larger, where for example for KAGA and KAGA*, we obtain uncertainties of 2.2 and 1.6 mm yr^{-1}, respectively. The noisy data from between August 2006 and March 2007 for KAGA therefore increases the uncertainty by almost a factor of two, although the uplift rate remains the same.

[23] If the noise is characterized by a fractal noise process with a spectral index of −0.65 (this value best matches the spectrum of our uplift time series), the uncertainties become almost the same as when using the FTM method. However, we note that the uncertainty at KAGA when using $\kappa = -0.65$ is slightly less than that obtained using the FTM method. This is mainly due to the fact that, compared to the MLE technique which uses equal weights, FTM downweights the noisy data between August 30, 2006 and March 14, 2007 since they have larger uncertainties. When the noisy data are removed and all individual daily solutions have more or less the same uncertainty, the FTM and Fractional Gaussian methods (with $\kappa = -0.65$) produce almost identical results.

5. Estimated Crustal Uplift due to Mass Loss From Jakobshavn Isbræ

[24] *Joughin et al.* [2008b] constructed several glacial surface elevation change maps between 1997–2002, 2002–2005, and 2005–2006, using ATM observations of Jakobshavn Isbræ. In this study, we use a more recent 2006–2009 elevation change map, based on ATM observations made during May 27–30, 2006 and April 27–28, 2009. This map thus covers roughly the same time span as the GPS data. Figure 5 shows the thinning rates between 2006 and 2009 over the grounded portion of Jakobshavn Isbræ, using a grid spacing of 1 km. The grounding line (the black line in Figure 5b) is determined from a post-2003 summer Radarsat image. Compared with the map of thinning rates during 2005–2006 [*Joughin et al.*, 2008b], we observe a decrease in thinning rates near the ice front as well as a

Table 5. Adjusted and Predicted Elastic Uplift Rates due to Unloading on Jakobshavn Isbræ[a]

	Adjusted at JI	Unloading on JI	Unloading Outside JI	PGR
KAGA	14.6 ± 1.7	12.1 ± 0.9	2.3 ± 0.4	−4.0 ± 0.5
ILUL	4.9 ± 1.1	3.2 ± 0.3	2.2 ± 0.4	−2.8 ± 0.5
QEQE	2.0 ± 1.0	1.2 ± 0.1	2.0 ± 0.4	−1.6 ± 0.5
AASI	1.4	1.4 ± 0.1	1.9 ± 0.4	−1.7 ± 0.5

[a]The adjusted uplift rates are obtained after subtracting the PGR signal and the elastic signal due to ice loss outside Jakobshavn Isbræ, and subtracting an uplift rate of 4.2 mm yr^{-1} from each station. Since by subtracting 4.2 mm yr^{-1}, we constrain the observed uplift rate at AASI to the predicted rate, we map the uncertainties at AASI to those at the other sites. Predicted uplift rates in mm yr^{-1} due to the melting or unloading of Jakobshavn Isbræ (JI), unloading outside JI, and PGR (PGR uncertainties are not listed here but are discussed in section 7). Uplift rates are in mm yr^{-1}.

propagation of thinning towards the interior. These two changes are consistent with one another, since inland acceleration decreases the rate of stretching and thinning at the front, as is observed.

[25] By assuming that the thinning is due to the loss of ice with a density of 910 kg m^{-3}, the same value used by *Joughin et al.* [2008b], we transform the ATM elevation changes into gridded mass loss values. Following *Joughin et al.*'s [2008b] error budget, we assign the same uncertainty value (±0.21 m yr^{-1}) to the thinning rate at all grid points (1 km spacing). This uncertainty originates from two sources: errors in ATM altimetry measurements (~±10 cm for each individual elevation measurement) and errors in the assumed density caused by inter-annual surface mass variability [*Joughin et al.*, 2008b; *Howat et al.*, 2008]. We use the value of 0.56 m yr^{-1}, given by *Joughin et al.* [2008b] and based on the work of *van de Wal et al.* [2005], to represent the inter-annual variation of surface mass balance (SMB). Scaling this SMB uncertainty by the ratio of ice and water density, as well as by the time interval between two ATM measurements (three years in this case), we calculate the uncertainty in the thinning rate due to the inter-annual variability of the SMB. We add the altimetry measurement uncertainty and the SMB uncertainties in quadrature to obtain a value of 0.21 m yr^{-1} for the uncertainty in the ATM thinning rates for 2006–2009.

[26] Using the same grounded area reported by *Joughin et al.* [2008b] for previous years, we estimate a net 2006–2009 ice loss of 22 ± 2 km^3 yr^{-1}, which is about the same as the 2005–2006 rate [*Joughin et al.*, 2008b]. This could be an under-estimation of the total loss over the catchment, as the area of dynamic thinning may have spread some distance inland of the ATM survey grid. Also note that the uncertainty in the net ice loss estimate is smaller than that obtained using equation (1) of *Joughin et al.* [2008b], because the uncertainty in their study is attributed to the components of dynamic thinning only, while in our work it is attributed to the total loss of ice mass.

[27] We convolve the gridded thinning rates and their uncertainties with *Farrell*'s [1972] vertical-displacement Green's function, to calculate crustal uplift at the GPS sites in response to Jakobshavn Isbræ ice mass loss. The predicted uplift rates are (Table 5): 12.1 ± 0.9 mm yr^{-1} (KAGA), 3.2 ± 0.3 mm yr^{-1} (ILUL), 1.2 ± 0.1 mm yr^{-1} (QEQE), and 1.4 ± 0.1 mm yr^{-1} (AASI).

6. Constraining the Observed GPS Uplift

6.1. Other Contributions to Crustal Uplift

[28] To compare GPS results with the predicted rates based on ATM estimates (given in section 5), we must isolate the part of the loading signal caused by mass changes in Jakobshavn Isbræ and its catchment. That requires minimizing contamination from other contributions.

[29] We use the global ice-change model ICE-5G of *Peltier* [2004] to predict post-glacial rebound (PGR) caused by the Earth's viscoelastic response to past ice mass variability. ICE-5G predicts PGR uplift rates of −4.0 mm yr^{-1} (KAGA), −2.8 mm yr^{-1} (ILUL), −1.6 mm yr^{-1} (QEQE), and −1.7 mm yr^{-1} (AASI) (also listed in Table 5), which are subtracted from the GPS rates. They are all negative (indicating subsidence) largely because ICE-5G includes a late Holocene re-advance of the west Greenland ice-sheet margin into this region over the last 7500 years (PGR rates and their errors are discussed further in section 7), as well as the effect of the ongoing collapse of the forebuldge that surrounded the former Laurentide ice sheet.

[30] The GPS results could also include contributions from loading outside the Jakobshavn Isbræ drainage basin. There has, for example, been recent thinning in other Greenland glacial drainage basins [e.g., *Krabill et al.*, 1999, 2004; *Stearns and Hamilton*, 2007; *Howat et al.*, 2008; *Velicogna*, 2009], and deformation caused by these mass variations could be affecting our GPS trend solutions. To assess the contributions from these loading signals, we note that because the loads are distant from the four GPS stations, their effects would likely be about the same at each station. For example, by convolving *Farrell*'s [1972] Green's function with *Velicogna*'s [2009] mass loss estimate for Greenland (excluding the Jakobshavn Isbræ basin) between 2007–2009 of 286 ± 50 Gt yr^{-1}, we obtain loading signals at our sites of 2.3 ± 0.4 mm yr^{-1} (KAGA), 2.2 ± 0.4 mm yr^{-1} (ILUL), 2.0 ± 0.4 mm yr^{-1} (QEQE), and 1.9 ± 0.4 mm yr^{-1} (AASI) (listed in Table 5). We use a slightly larger uncertainty than *Velicogna* [2009] because of the different time span of the GPS data (2006–2009). Figure 6 shows the mass loss rates used to calculate the elastic loading signal.

[31] In contrast to the contributions from distant loads and from the long-period GPS errors, the loading signals from Jakobshavn Isbræ (second column in Table 5) differ significantly between the four stations, as is evident from the estimates presented in section 4. Figure 5 shows that Jakobshavn Isbræ is thinning mainly near the calving front. The predicted 12.1 ± 0.9 mm yr^{-1} uplift at KAGA is mostly due to this nearby thinning. The estimated uplift decreases rapidly to only 3.2 ± 0.3 mm yr^{-1} at ILUL. The even smaller predicted rates of 1.2 ± 0.1 mm yr^{-1} and 1.4 ± 0.1 mm yr^{-1} at QEQE and AASI would not be affected much if the modeled thinning near the front were incorrect.

6.2. Uplift Relative to AASI

[32] To interpret these GPS results, this study focuses on uplift at KAGA, ILUL, and QEQE relative to AASI. By considering relative displacements rather than absolute geocentric displacements, we effectively remove contributions

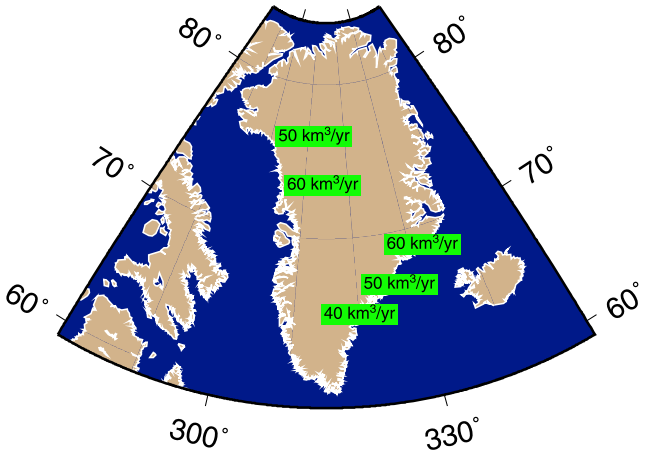

Figure 6. Greenland ice mass loss rates used to calculate the elastic loading signal due to mass loss outside of the Jakobshavn Isbræ drainage basin.

from frame uncertainty and frame drift. Additionally, troposphere error, unmodeled orbit errors, ice load errors from outside the Jakobshavn Isbræ catchment, and PGR errors are reduced when relative displacements over short distances are considered.

[33] The GPS measurements at AASI suggest an absolute uplift rate of 5.8 ± 0.5 mm yr^{-1}. The sum of the predicted uplift rates due to PGR (−1.7 mm yr^{-1}), from the thinning of Jakobshavn Isbræ (1.4 mm yr^{-1}), and from unloading outside of the Jakobshavn Isbræ drainage basin (1.9 mm yr^{-1}) is 1.6 mm yr^{-1}, resulting in a difference between the observed and predicted absolute uplift rates of 5.8 − 1.6 = 4.2 mm yr^{-1}, which is presumably due to a combination of unmodeled orbit errors, reference frame errors, ice load errors, and PGR errors (see section 7).

[34] We subtract a uniform uplift rate of 4.2 mm yr^{-1} from each station's data. The orbit and reference frame errors, as well as errors in our estimates of loading from outside the Jakobshavn Isbræ catchment, are likely to be essentially the same at each GPS station. Thus, by subtracting the AASI rate, we effectively remove those errors from the rates of all the stations. This subtraction also removes, from every station, the error in our estimates of Jakobshavn Isbræ loading at AASI. Therefore, in effect we are implicitly assuming that the AASI uplift rate due to Jakobshavn Isbræ is well predicted by the surface elevation change map based on ATM observations.

[35] The second column in Table 5 lists the adjusted uplift rates at KAGA, ILUL, QEQE, and AASI computed after subtracting the PGR signal and the elastic signal due to ice-mass loss outside of Jakobshavn Isbræ, and removing an uplift rate of 4.2 mm yr^{-1} from each station's data to constrain the observed GPS uplift to the estimated AASI uplift, leaving the contribution from the Jakobshavn Isbræ. Thus, the second and third columns in Table 5 present the observed and predicted uplift rates due to unloading on Jakobshavn Isbræ and its catchment, respectively. Because we constrain the GPS-observed elastic rate at AASI to the predicted value based on ATM measurements, we quadratically add the uncertainties in the observed rate at AASI (due to errors in the GPS rate estimates and in the estimated elastic rates due to ice loss outside of Jakobshavn Isbræ) to the uncertainties in the rates at KAGA, ILUL, and QEQE. We also quadratically add our estimated errors in the PGR gradients (see below) to the uncertainties at these three sites. Similarly, we quadratically add the uncertainties in the predicted rate at AASI to the uncertainties in the predicted rates at the other three sites. We note that within the uncertainty levels, the GPS-observed uplift rates at KAGA, ILUL, and QEQE agree with the predictions based on the ATM measurements.

7. Estimating PGR Uncertainties

[36] In this section, we estimate the uncertainties associated with the ICE-5G PGR rates at the four GPS sites (see Table 5 and section 6), and discuss the impact that PGR errors might have on our estimates of the elastic uplift rates caused by the thinning of Jakobshavn Isbræ. The present-day PGR deformation depends on the global deglaciation history and the Earth's viscoelastic structure. Errors in either of those would therefore introduce errors into the predicted PGR rates. In the following subsections, we assess the PGR uncertainties from these two sources separately.

[37] To estimate the PGR corrections given in Table 5, we spatially interpolated results for the ICE-5G ice history and VM2 viscosity profile, as computed by W.R. Peltier and available publicly at http://www.sbl.statkart.no/projects/pgs/displacements. To estimate the uncertainties in those results, we use a simpler glacial-rebound model than was employed by *Peltier* [2004]. Specifically, we assume an incompressible Earth, consisting of a homogeneous elastic lithosphere, a Maxwell viscoelastic mantle divided into two homogeneous layers (upper and lower mantles), and a homogeneous inviscid core, and we ignore ocean loading and rotational feedback. We obtain reference uplift rates by running our simplified model using the ICE-5G deglaciation history and a two-layer approximation to the VM2 viscosity profile [*Peltier*, 2004]. We obtain other uplift rates by running our model with a variety of alternative deglaciation histories and viscosity profiles, and use the differences between these other values and our reference values to obtain an estimate of the uncertainties in the original ICE-5G/VM2 results. Our underlying assumption is that the numerical effects of changing the ice history or viscosity profile for our simplified model are roughly the same as changing them for a more complete PGR model.

7.1. PGR Uncertainties due to Errors in the Earth's Viscoelastic Structure

[38] To assess PGR uncertainties due to possible errors in the VM2 viscoelastic structure, we use our simplified model to calculate and compare present-day PGR rates caused by the global ICE-5G ice model [*Peltier*, 2004] for the range of viscosity profiles listed in Table 6. Our reference viscoelastic model (Model Ref, Table 6), is a two-layer approximation to *Peltier*'s [1996] VM2 model, except that our lithospheric thickness is only 90 km [see *Peltier*, 2004]. Model 1 is another two-layer approximation for VM2, with a thicker lithosphere (120 km) and a thinner upper mantle than Model Ref. Model 2 is a two-layer approximation for the M1 model described by *Peltier* [1996]. We construct models 3–5 to represent a range of feasible mantle viscos-

Table 6. Viscoelastic Models We Use to Estimate the Corrections to PGR Rates due to Possible Errors in the ICE-5G Viscoelastic Structure[a]

	Outer Radius (km)	Shear Wave Speed (km/s)	Density (g/cm^3)	Viscosity ($\times 10^{21}$ Pa-sec)
		Model Ref		
Core	3485.	0.0	12.200	-
Lower mantle	5201.	6.687	4.963	3.6
Upper mantle	6281.	4.676	3.515	0.9
Lithosphere	6371.	4.676	3.515	-
		Model 1		
Core	3485.	0.0	12.200	-
Lower mantle	5201.	7.000	4.963	3.5
Upper mantle	6250.	5.400	4.000	0.87
Lithosphere	6371.	3.700	3.000	-
		Model 2		
Core	3485.	0.0	12.200	-
Lower mantle	5701.	6.687	4.963	2.0
Upper mantle	6251.	4.676	3.515	1.0
Lithosphere	6371.	4.676	3.515	-
		Model 3		
Core	3485.	0.0	12.200	-
Lower mantle	5701.	6.687	4.963	4.0
Upper mantle	6251.	4.676	3.515	0.6
Lithosphere	6371.	4.676	3.515	-
		Model 4		
Core	3485.	0.0	12.200	-
Lower mantle	5701.	6.687	4.963	10.0
Upper mantle	6251.	4.676	3.515	1.0
Lithosphere	6371.	4.676	3.515	-
		Model 5		
Core	3485.	0.0	12.200	-
Lower mantle	5701.	6.687	4.963	50.0
Upper mantle	6251.	4.676	3.515	1.0
Lithosphere	6371.	4.676	3.515	-

[a]See section 7.1. For each model we assume an inviscid core and an elastic lithosphere.

ities. Model 3 represents an example of low viscosities in both the upper and lower mantle; Model 5 represents high viscosities in the lower mantle. Strictly speaking, it is inconsistent to combine the ICE-5G ice model with a viscosity profile that was not used in its development, since the ice model was originally constructed so that, when used with that viscosity profile, it would predict PGR observables (e.g., relative sea level variations). Hence there is some dependence between the ice-sheet history and the viscoelastic model. There is no guarantee that the model would successfully predict those observations with another viscosity profile. Still, the comparisons described here do provide some insight into the sensitivity of the uplift to the Earth's structure.

[39] Table 7 lists our present-day uplift rates at the four GPS sites, computed using these viscoelastic models. We compare the Model Ref results with the other five sets of rates from two perspectives: the difference at AASI, and the differences in the spatial gradients (i.e., differences between stations, not differences per unit distance) between the other sites (KAGA, ILUL, and QEQE) and AASI (listed in parentheses in Table 7). The errors in these spatial gradients that are most pertinent to the GPS results shown in Table 5, since the error in the AASI PGR rate has been implicitly removed from those results. First, relative to the rate based on Model Ref, the difference in AASI's rate (last row in Table 7) ranges from −3.5 mm yr^{-1} to −0.7 mm yr^{-1}. Therefore, if we assume that one of the other models besides Model Ref is correct, we would add a value of between −3.5 mm yr^{-1} and −0.7 mm yr^{-1} to the AASI PGR rate shown in Table 5. This range of values is not symmetric about 0, and suggests that we view this contribution to the AASI uncertainty as a possible bias of up to 3.5 mm/yr. Second, different viscoelastic structures cause relatively small changes in the PGR gradients. For example, relative to the KAGA-AASI gradient based on Model Ref, the differences in this gradient range from −0.4 mm yr^{-1} to 0.3 mm yr^{-1}. Therefore, the correction to the KAGA-AASI PGR gradient is about ±0.4 mm yr^{-1}, which can be treated as a formal error. Based on the range of the corrections to the PGR gradients, we assign ±0.5 mm yr^{-1} as the uncertainty in the PGR gradients.

7.2. PGR Uncertainties due to Errors in the Ice History Model

[40] PGR deformation at our Greenland GPS sites is caused by Pleistocene/Holocene ice variability both from within Greenland and from without (e.g., North America and Scandinavia). The contributions from both regions are important. However, it is likely that errors in the Greenland component of the deglaciation model would have a greater impact on our results than errors in the North American or Scandinavian components, as the Greenland Ice Sheet is obviously much closer to our GPS sites than the other ice masses. Furthermore, the Greenland Ice Sheet apparently underwent dramatic changes much more recently than the other ice sheets. This implies that the PGR estimates for our GPS sites are probably much more dependent on the spatial and temporal details of Greenland's glacial history than of North America or Scandinavia, and so they are probably more susceptible to errors in Greenland's deglaciation model.

[41] To assess the errors in the computed PGR rates due to possible errors in ICE-5G's Greenland deglaciation component, we use three Greenland ice histories: (1) the ICE-5G Greenland ice history (as our default model), (2) ICE-5G but with no Greenland ice variations after 7500 years before

Table 7. Present-Day PGR Uplift Rates, Computed for Different Viscoelastic Models[a]

	Model Ref	Model 1	Model 2	Model 3	Model 4	Model 5	Range of Correction
KAGA	−0.1 (−0.3)	−0.9 (−0.4)	−1.4 (−0.1)	−4.0 (−0.7)	−1.3 (−0.2)	−0.8 (0.0)	(−0.4) ~ (0.3)
ILUL	0.1 (−0.1)	−0.7 (−0.2)	−1.4 (−0.1)	−3.8 (−0.5)	−1.3 (−0.2)	−0.8 (0.0)	(−0.4) ~ (0.1)
QEQE	0.5 (0.3)	−0.5 (0.0)	−1.4 (−0.1)	−3.1 (0.2)	−1.2 (−0.1)	−1.0 (−0.2)	(−0.5) ~ (−0.1)
AASI	0.2 (—)	−0.5 (—)	−1.3 (—)	−3.3 (—)	−1.1 (—)	−0.8 (—)	−3.5 ~ −0.7

[a]The gradients (differences between PGR rates) between KAGA/ILUL/QEQE and AASI are listed in parentheses. The eighth column lists the range of corrections to the PGR gradients and to the AASI rates, all relative to the Model Ref results. Uplift rates are in mm yr^{-1}.

Table 8. Present-Day PGR Uplift Rates Caused by Ice Variability on the Greenland Ice Sheet Alone, Computed Using Different Greenland Ice History Models[a]

	ICE-5G*	ICE-5G**	Fleming and Lambeck
KAGA	1.7 (−0.7)	7.9 (0.9)	4.3 (0.4)
ILUL	2.0 (−0.4)	7.6 (0.6)	4.1 (0.2)
QEQE	2.4 (0.0)	6.1 (−0.9)	3.3 (−0.4)
AASI	2.4 (—)	7.0 (—)	3.9 (—)

[a]ICE-5G*: ICE-5G Greenland ice history; ICE-5G**: ICE-5G Greenland ice history, but stopped 7500 years BP; Fleming and Lambeck: The Greenland ice history without a post-7500 years BP component i.e. no readvance. The gradients between KAGA/ILUL/QEQE and AASI are listed in parentheses. Uplift rates are in mm yr^{-1}.

present (BP) (see section 7.2.1), and (3) the independent Greenland ice model of *Fleming and Lambeck* [2004] (hereafter referred to as Fleming and Lambeck). We use these Greenland ice histories together with the PGR model described in section 7.1 and the Model Ref viscoelastic parameters, to compute and compare present-day PGR rates.

7.2.1. Uncertainties due to Errors in the Late Holocene Ice History

[42] ICE-5G predicts present-day subsidence at the four GPS sites, largely because of ice sheet re-advance in western Greenland during the last 7500 years of the Holocene [*Wahr et al.*, 2001; *Tarasov and Peltier*, 2002]. However, details of this re-glaciation are still highly uncertain. To determine the impact this readvance has on our PGR uplift estimates, we construct a Greenland ice history model (denoted as ICE-5G**) that is identical to ICE-5G before 7500 BP, but where we omit all ice variability after 7500 years BP (that is, the readvance is not included). The original Greenland component of ICE-5G Greenland, including the modeled readvance after 7500 years BP, is denoted here as ICE-5G*. Table 8 lists the calculated present-day uplift rates using ICE-5G* and ICE-5G**. The difference represents the total effects of ICE-5G's Holocene readvance, and we interpret that difference as an upper bound for the errors caused by possibly mismodeling that readvance.

[43] As before, we study both the change in the PGR rate at AASI, and the PGR gradients between AASI and the other three sites. First, Table 8 shows that the ICE-5G Greenland re-advance is responsible for a subsidence of 4.6 mm yr^{-1} at AASI (2.4 mm yr^{-1} uplift minus 7.0 mm yr^{-1} uplift). Thus, if we made the extreme assumption that there was no readvance during the last 7500 years, we would have to make a 4.6 mm yr^{-1} correction to the ICE-5G AASI PGR uplift rate. Second, the differences in the PGR gradients are 1.6 mm yr^{-1} (KAGA minus AASI), 1.0 mm yr^{-1} (ILUL minus AASI), and −0.9 mm yr^{-1} (QEQE minus AASI), respectively. We interpret these differences as upper bounds for the uncertainties in the gradients listed in Table 5, due to errors in the ICE-5G ice history since the late Holocene.

[44] We emphasize that this comparison almost certainly overestimates the uncertainties caused by a mismodeled ice re-advance, because (1) we use the entire readvance as the error source, and (2) we stop ICE-5G's ice history at 7500 years BP, when the ice volume was smaller than the present-day volume and when the west Greenland ice margin to the south had retreated inland of the present-day ice margin by the order of 50 km [e.g., *van Tatenhove et al.*, 1996; *Wahr et al.*, 2001]. Because of (2), the ICE-5G** model overestimates the deglaciation that would have occurred prior to 7500 years ago if there had been no later readvance.

7.2.2. PGR Uncertainties due to Errors in the Ice History Prior to the Holocene

[45] We also estimate the PGR errors due to errors in the ice history before the ice sheet re-advance, by comparing ICE-5G** and Fleming and Lambeck's ice models before 7500 years BP. The calculated PGR rates based on Fleming and Lambeck are listed in the fourth column of Table 8. At AASI, Fleming and Lambeck predicts 3.1 mm yr^{-1} less uplift than ICE-5G** (3.9 mm yr^{-1} minus 7.0 mm yr^{-1}). The differences in gradients between AASI and the other three GPS sites due to the errors in ice history before 7500 years are relatively small. For example, using Fleming and Lambeck as a reference, ice model errors in ICE-5G cause an uplift PGR gradient of 0.5 mm yr^{-1} between KAGA and AASI.

[46] The preceding ice history uncertainty estimates only consider errors in the Greenland ice component. To estimate the uncertainties due to possible errors in the ice components of other regions (e.g., Canada and Scandinavia), we use a spectral-finite element method of *Martinec* [2000] to calculate present-day PGR rates using: (1) global ICE-5G with the VM2 structure; (2) the global ICE-5G model but stopped at 7500 years BP; and (3) the global ice model, including Greenland, as used by *Fleming and Lambeck* [2004], as well as the viscoelastic structure used in that work (lithosphere thickness of 80 km, upper and lower mantle viscosities of 5×10^{20} Pas and 1×10^{22} Pas, respectively). Comparing results for (1) and (2), and for (2) and (3) (numerical values not given here), we find that the differences are similar to those obtained by comparing just the Greenland components, as described above.

7.3. Effects of All PGR Errors on the Estimated Elastic Uplift

[47] In the paragraphs above, we estimated the uncertainties in the ICE-5G PGR rates. When comparing the observed GPS uplift rates with the elastic uplift rates predicted for ice unloading from Jakobshavn Isbræ, we first subtracted the PGR rates, and then removed a common error of 4.2 mm yr^{-1} (see section 6). This value for the common error was chosen so that the GPS results at AASI are in perfect agreement with the predictions for Jakobshavn Isbræ thinning.

[48] The calculations in sections 7.1 and 7.2 suggest the following: (1) Errors in the viscoelastic structure could conceivably lead to small errors in the estimated PGR gradients that could have either sign. We assign an uncertainty of ±0.5 mm yr^{-1} to the PGR gradients, and add it quadratically to the uncertainties in the GPS-observed elastic rates at KAGA, ILUL, and QEQE (Table 5); (2) errors in the ice history could cause our PGR correction for KAGA-AASI to be overestimated by up to 1.6 mm yr^{-1}. As discussed in section 7.2.1, however, we have almost certainly overestimated these errors, and we do not include them in the formal uncertainty estimates. We note though, that if we were to correct the observed GPS gradients for these errors (i.e. for the differences between the ICE-5G** and ICE-5G* values in Table 8), it would improve the agreement between the predicted rates and the GPS-derived elastic uplift rates at

KAGA and ILUL. The agreement at QEQE would become worse, but would still lie within the uncertainty limits; (3) the error in the PGR rate at AASI contributes to the 4.2 mm yr^{-1} common error we subtracted from the GPS uplift rates, as do errors associated with orbits, atmospheric corrections, reference frame, and loading in Greenland's interior (section 6). Our PGR results show that the PGR error at AASI could be up to 4 mm yr^{-1}, either uplift or subsidence, and so could explain a large portion of the common error constant.

8. Discussion and Conclusions

[49] We have analyzed data from four continuously operating GPS receivers located between 5 and 150 km from the Jakobshavn Isbræ terminus. The GPS uplift rates are large near the front, but decrease dramatically as the distance from the glacier increases. This spatial dependence strongly suggests that the differential uplift is caused by Jakobshavn Isbræ mass loss. The GPS measurements indicate crustal uplift rates caused by the thinning of Jakobshavn Isbræ and its catchment, of 14.6 ± 1.7 mm yr^{-1} (KAGA), 4.9 ± 1.1 mm yr^{-1} (ILUL), 2.1 ± 1.0 mm yr^{-1} (QEQE), and 1.4 mm yr^{-1} (AASI). The rate at KAGA, the station closest to Jakobshavn Isbræ, is large and supports evidence from other sources [e.g., *Rignot and Kanagaratnam*, 2006] that Jakobshavn Isbræ is losing mass and unloading the crust at a considerable rate.

[50] We have used these results as independent constraints on the surface mass balance estimates from altimetry surveys. To isolate the part of the loading signal caused by mass changes of Jakobshavn Isbræ and its catchment, we use models, such as the postglacial rebound model ICE-5G [*Peltier*, 2004] and the Greenland ice mass loss model from *Velicogna* [2009], to remove contamination from other processes. When constraining the observed GPS uplift rates to the elastic uplift rates exclusively due to ice unloading from Jakobshavn Isbræ, we subtract a common error of 4.2 mm yr^{-1}. The common error is due to a combination of a spatially-uniform error in the PGR rate, orbit errors, atmospheric errors, reference frame errors, and errors in loading changes from the other parts of Greenland. Based on our analysis of PGR errors (arising from uncertainties in the Earth's viscoelastic structure and assumed ice history model) we assign an uncertainty of ±0.5 mm yr^{-1} to the PGR gradients, and add it quadratically to the uncertainties in the GPS-observed elastic rates at KAGA, ILUL, and QEQE. We also assign an uncertainty of ±0.4 mm yr^{-1} due to loading outside the Jakobshavn Isbræ drainage basin and add it quadratically to the uncertainties in the GPS-observed rates.

[51] The observed uplift rates are compared with predicted rates computed using thinning estimates from ATM laser altimetry (Table 1). The observations are all slightly larger than the predictions at KAGA, ILUL, and QEQE. But in each case, the observations and predictions agree to within the uncertainty levels. We note that a modeled underestimation at every station could be partially explained by the fact that the ice thinning map produced using ATM measurements underestimates the total ice mass loss within the entire Jakobshavn Isbræ catchment since the area of dynamic thinning has spread inland of the ATM survey grid.

[52] The GNET project [*Bevis*, 2009], which is part of the International Polar Year (IPY) POLENET (Polar Earth Observation Network) consortium and includes participation from Denmark, Luxembourg, and the USA, coordinated the installation of about 40 new permanent bedrock GPS stations between 2007 and 2009. By using this greatly expanded network of GPS stations positioned all around the edge of the Greenland Ice Sheet, it will be possible to use analysis techniques such as those described here to study the Earth's elastic response to mass unloading from the entire Greenland Ice Sheet, and to improve drainage-basin scale studies of many individual glaciers, as well as providing additional constraints for studies dealing with the ongoing adjustment of the Earth following the last glacial-interglacial period.

[53] **Acknowledgments.** We thank Finn Bo Madsen for access to the ILUL, AASI and QEQE data. We thank Bjorn Johns, Mark Fahnestock, and Martin Truffer for access to the KAGA data. KAGA was established by Mark Fahnestock and Martin Truffer and funded by NASA. Work at the University of Colorado was partially supported by NASA grant NNX06AH37G and JPL contract 1259025. Lin Liu was partially supported by a NASA Earth and Space Science Fellowship Program. We thank Zdenek Martinec (Dublin Institute of Advanced Studies) and Jan Hagedoorn (GFZ Potsdam) for allowing the use of their software. Kevin Fleming acknowledges the support of the Australian Research Council Discovery Project "Environmental geodesy: variations of sea level and water storage in the Australian region" (DP087738). We thank Christopher F. Larsen and one anonymous reviewer and the Associate Editor for constructive comments which helped improve the manuscript.

References

Altamimi, Z., X. Collilieux, J. Legrand, B. Garayt, and C. Boucher (2007), ITRF2005: A new release of the International Terrestrial Reference Frame based on time series of station positions and Earth Orientation Parameters, *J. Geophys. Res.*, *112*, B09401, doi:10.1029/2007JB004949.

Amundson, J. M., M. Fahnestock, M. Truffer, J. Brown, M. P. Luthi, and R. J. Motyka (2010), Ice melange dynamics and implications for terminus stability, Jakobshavn Isbræ, Greenland, *J. Geophys. Res.*, *115*, F01005, doi:10.1029/2009JF001405.

Agnew, D. C. (1992), The time-domain behavior of power-law noises, *Geophys. Res. Lett.*, *19*(4), 333–336.

Bevis, M. (2009), GNET—Using bedrock geodesy to constrain past and present day changes in Greenland's ice mass, paper presented at International Workshop on Changes in the Greenland Cryosphere, Natl. Space Inst., Tech. Univ. of Denmark, Nuuk, Greenland, 25–27 Aug.

Boehm, J., A. Niell, P. Tregoning, and H. Schuh (2006a), Global Mapping Function (GMF): A new empirical mapping function based on numerical weather model data, *Geophys. Res. Lett.*, *33*, L07304, doi:10.1029/2005GL025546.

Boehm, J., B. Werl, and H. Schuh (2006b), Troposphere mapping functions for GPS and very long baseline interferometry from European Centre for Medium-Range Weather Forecasts operational analysis data, *J. Geophys. Res.*, *111*, B02406, doi:10.1029/2005JB003629.

Clarke, T. S., and K. A. Echelmeyer (1996), Seismic-reflection evidence for a deep subglacial trough beneath Jakobshavns Isbræ, West Greenland, *J. Glaciol.*, *43*(141), 219–232.

Davis, J. L., B. P. Wernicke, S. Bisnath, N. A. Niemi, and P. Elosegui (2006), Subcontinental-scale crustal velocity changes along the Pacific–North America plate boundary, *Nature*, *441*, 1131–1134, doi:10.1038/nature04781.

Dietrich, R., H.-G. Maas, M. Baessler, A. Rulke, A. Richter, E. Schwalbe, and P. Westfeld (2007), Jakobshavn Isbræ, West Greenland: Flow velocities and tidal interaction of the front area from 2004 field observations, *J. Geophys. Res.*, *112*, F03S21, doi:10.1029/2006JF000601.

Dietrich, R., E. Ivins, G. Casassa, H. Lange, J. Wendt, and M. Fritsche (2010), Rapid crustal uplift in Patagonia due to enhanced ice loss, *Earth Planet. Sci. Lett.*, *289*(1–2), 22–29, doi:10.1016/j.epsl.2009.10.021.

Farrell, W. (1972), Deformation of the Earth by surface loads, *Rev. Geophys.*, *10*, 761–797.

Fleming, K., and K. Lambeck (2004), Constraints on the Greenland Ice Sheet since the Last Glacial Maximum from sea-level observations and glacial-rebound models, *Quat. Sci. Rev.*, *23*, 1053–1077, doi:10.1016/j.quascirev.2003.11.001.

Holland, D. M., R. H. Thomas, B. de Young, M. H. Ribergaard, and B. Lyberth (2008), Acceleration of Jakobshavn Isbræ triggered by warm subsurface ocean waters, *Nat. Geosci.*, *1*, 659–664, doi:10.1038/ngeo316.

Howat, I. M., B. E. Smith, I. Joughin, and T. A. Scambos (2008), Rates of southeast Greenland ice volume loss from combined ICESat and ASTER observations, *Geophys. Res. Lett.*, *35*, L17505, doi:10.1029/2008GL034496.

Johansson, J. M., et al. (2002), Continuous GPS measurements of post-glacial adjustment in Fennoscandia: 1. Geodetic results, *J. Geophys. Res.*, *107*(B8), 2157, doi:10.1029/2001JB000400.

Joughin, I., W. Abdalati, and M. Fahnestock (2004), Large fluctuations in speed on Greenland's Jakobshavn glacier, *Nature*, *432*, 608–610, doi:10.1038/nature03130.

Joughin, I., S. B. Das, M. A. King, B. E. Smith, I. M. Howat, and T. Moon (2008a), Seasonal speedup along the western flank of the Greenland Ice Sheet, *Science*, *320*(5877), 781–783, doi:10.1126/science.1153288.

Joughin, I., I. M. Howat, M. Fahnestock, B. Smith, W. Krabill, R. B. Alley, H. Stern, and M. Truffer (2008b), Continued evolution of Jakobshavn Isbræ following its rapid speedup, *J. Geophys. Res.*, *113*, F04006, doi:10.1029/2008JF001023.

Khan, S. A., J. Wahr, L. A. Stearns, G. S. Hamilton, T. van Dam, K. M. Larson, and O. Francis (2007), Elastic uplift in southeast Greenland due to rapid ice mass loss, *Geophys. Res. Lett.*, *34*, L21701, doi:10.1029/2007GL031468.

Khan, S. A., J. Wahr, E. Leuliette, T. van Dam, K. M. Larson, and O. Francis (2008), Geodetic measurements of postglacial adjustments in Greenland, *J. Geophys. Res.*, *113*, B02402, doi:10.1029/2007JB004956.

Khan, S. A., J. Wahr, M. Bevis, I. Velicogna, and E. Kendrick (2010), Spread of ice mass loss into northwest Greenland observed by GRACE and GPS, *Geophys. Res. Lett.*, *37*, L06501, doi:10.1029/2010GL042460.

Larsen, C. F., R. J. Motyka, J. T. Freymueller, K. A. Echelmeyer, and E. R. Ivins (2004), Rapid uplift of southern Alaska caused by recent ice loss, *Geophys. J. Int.*, *158*, 1118–1133, doi:10.1111/j.1365-246X.2004.02356.x.

Larsen, C. F., R. J. Motyka, J. T. Freymueller, K A. Echelmeyer, and E. R. Ivins (2005), Rapid viscoelastic uplift in southeast Alaska caused by post-Little Ice Age glacial retreat, *Earth Planet. Sci. Lett.*, *237*, 548–560, doi:10.1016/j.epsl.2005.06.032.

Krabill, W., E. Frederick, S. Manizade, C. Martin, J. Sonntag, R. Swift, R. Thomas, W. Wright, and J. Yungel (1999), Rapid thinning of parts of the southern Greenland Ice Sheet, *Science*, *283*(5407), 1522–1524, doi:10.1126/science.283.5407.1522.

Krabill, W., W. Abdalati, E. Frederick, S. Manizade, C. Martin, J. Sonntag, R. Swift, R. Thomas, W. Wright, and J. Yungel (2000), Greenland Ice Sheet: Increased coastal thinning, *Science*, *289*, 428–430.

Krabill, W., et al. (2004), Greenland Ice Sheet: Increased coastal thinning, *Geophys. Res. Lett.*, *31*, L24402, doi:10.1029/2004GL021533.

Mandelbrot, B. (1983), *The Fractal Geometry of Nature*, 466 pp., W. H. Freeman, San Francisco, Calif.

Mandelbrot, B., and J. van Ness (1968), Fractional Brownian motions, fractional noises and applications, *SIAM Rev.*, *10*, 422–439.

Martinec, Z. (2000), Spectral-finite element approach to three-dimensional viscoelastic relaxation in a spherical earth, *Geophys. J. Int.*, *142*, 117–141.

Niell, A. E. (1996), Global mapping functions for the atmosphere delay at radio wavelengths, *J. Geophys. Res.*, *101*(B2), 3227–3246.

Peltier, W. R. (1996), Mantle viscosity and ice-age ice sheet topography, *Science*, *273*, 1359–1364.

Peltier, W. R. (2004), Global glacial isostasy and the surface of the ice-age Earth: The ICE-5G (VM2) model and GRACE, *Annu. Rev. Earth Planet. Sci.*, *32*, 111–149.

Ray, R. (1999), A global ocean tide model from T/P altimetry: GOT99.2, *NASA Tech. Memo., 209478*.

Rignot, E., and P. Kanagaratnam (2006), Changes in the velocity structure of the Greenland Ice Sheet, *Science*, *311*, 986–990, doi:10.1126/science.1121381.

Rignot, E., J. E. Box, E. Burgess, and E. Hanna (2008), Mass balance of the Greenland ice sheet from 1958 to 2007, *Geophys. Res. Lett.*, *35*, L20502, doi:10.1029/2008GL035417.

Sato, T., J. Okuno, J. Hinderer, D. S. MacMillan, H. P. Plag, O. Francis, R. Falk, and Y. Fukuda (2006), A geophysical interpretation of the secular displacement and gravity rates observed at Ny-Alesund, Svalbard in the Arctic—Effects of post-glacial rebound and present-day melting, *Geophys. J. Int.*, *165*, 729–743.

Sauber, J. M., and B. F. Molnia (2004), Glacier ice mass fluctuations and fault instability in tectonically active Southern Alaska, *Global Planet. Change*, *42*, 279–293.

Soluri, E. A., and V. A. Woodson (1990), World vector shoreline, *Int. Hydrogr. Rev.*, *68*, 27–36.

Stearns, L. A., and G. S. Hamilton (2007), Rapid volume loss from East Greenland outlet glaciers quantified using repeat stereo satellite imagery, *Geophys. Res. Lett.*, *34*, L05503, doi:10.1029/2006GL028982.

Tarasov, L., and W. R. Peltier (2002), Greenland glacial history and local geodynamic consequences, *Geophys. J. Int.*, *150*, 198–229.

Teferle, F. N., S. D. P. Williams, H. P. Kierulf, R. M. Bingley, and H.-P. Plag (2008), A continuous GPS coordinate time series analysis strategy for high-accuracy vertical land movements, *Phys. Chem. Earth*, *33*, 205–216, doi:10.1016/j.pce.2006.11.002.

Thomas, R. H. (2004), Force-perturbation analysis of recent thinning and acceleration of Jakobshavn Isbræ, Greenland, *J. Glaciol.*, *50*(168), 57–66, doi:10.3189/172756504781830321.

Thomas, R. H., E. Frederick, W. Krabill, S. Manizade, and C. Martin (2009), Recent changes on Greenland outlet glaciers, *J. Glaciol.*, *55*(189), 57–66, doi:10.3189/172756504781830321.

Tregoning, P., and T. A. Herring (2006), Impact of a priori zenith hydrostatic delay errors on GPS estimates of station heights and zenith total delays, *Geophys. Res. Lett.*, *33*, L23303, doi:10.1029/2006GL027706.

van de Wal, R. S. W., W. Greuell, M. Van den Broeke, C. H. Reijmer, and J. Oerlemans (2005), Surface mass-balance observations and automatic weather station data along a transect near Kangerlussuaq, west Greenland, *Ann. Glaciol.*, *42*, 311–316, doi:10.3189/172756405781812529.

van Tatenhove, F., J. van der Meer, and E. Koster (1996), Implications for deglaciation chronology from new AMS age determinations in central West Greenland, *Quat. Res.*, *45*, 245–253.

Velicogna, I. (2009), Increasing rates of ice mass loss from the Greenland and Antarctic ice sheets revealed by GRACE, *Geophys. Res. Lett.*, *36*, L19503, doi:10.1029/2009GL040222.

Vey, S., R. Dietrich, M. Fritsche, A. Rulke, M. Rothacher, and P. Steigenberger (2006), Influence of mapping function parameters on global GPS network analyses: Comparisons between NMF and IMF, *Geophys. Res. Lett.*, *33*, L01814, doi:10.1029/2005GL024361.

Wahr, J., T. van Dam, K. M. Larson, and O. Francis (2001), Geodetic measurements in Greenland and their implications, *J. Geophys. Res.*, *106*(B8), 16,567–16,582.

Wdowinski, S., Y. Bock, J. Zhang, P. Fang, and J. Genrich (1997), Southern California permanent GPS Geodetic Array: Spatial filtering of daily positions for estimating coseismic and postseismic displacements induced by the 1992 Landers earthquake, *J. Geophys. Res.*, *102*(B8), 18,057–18,070.

Williams, S. D. P., Y. Bock, P. Fang, P. Jamason, R. M. Nikolaidis, L. Prawirodirdjo, M. Miller, and D. J. Johnson (2004), Error analysis of continuous GPS position time series, *J. Geophys. Res.*, *109*, B03412, doi:10.1029/2003JB002741.

Zumberge, J. F., M. B. Heflin, D. C. Jefferson, M. M. Watkins, and F. H. Webb (1997), Precise point positioning for the efficient and robust analysis of GPS data from large networks, *J. Geophys. Res.*, *102*, 5005–5017.

K. Fleming, Department of Spatial Sciences, Curtin University of Technology, Perth, WA 6845, Australia. (K.Fleming@curtin.edu.au)

I. Howat, School of Earth Sciences, Ohio State University, Columbus, OH 43210, USA. (ihowat@gmail.com)

I. Joughin, Applied Physics Lab, University of Washington, Seattle, WA 98105, USA. (ian@apl.washington.edu)

S. A. Khan, DTU Space–National Space Institute, Department of Geodesy, DK-2100 Copenhagen Ø, Denmark. (abbas@space.dtu.dk)

L. Liu and J. Wahr, Department of Physics, University of Colorado at Boulder, Boulder, CO 80309, USA. (liulin523@gmail.com; john.wahr@gmail.com)

T. van Dam, Department of Physics and Material Sciences, University of Luxembourg, 162a, av. de la Fayencerie, L-1511 Luxembourg, Luxembourg. (tonie.vandam@uni.lu)